Asymmetric supercapacitor based on activated expanded graphite and Pinecone tree activated carbon with excellent stability

Farshad Barzegar [a,b]*, Abdulhakeem Bello [b], Julien K. Dangbegnon [b], Ncholu Manyala [b]*, Xiaohua Xia [a]

* Farshad Barzegar: Tel.: +27 (0)12 420 4341; *E-mail address:* farshadbarzegar@gmail.com

* Ncholu Manyala: Tel: +27 (0)12 420 3549, Email address: ncholu.manyala@up.ac.za

[a] *Department of Electrical,Electronic and Computer Engineering, University of Pretoria, Pretoria 0002, South Africa*

[b] *Department of Physics, Institute of Applied Materials, SARCHI Chair in Carbon Technology and Materials, University of Pretoria, Pretoria 0028, South Africa.*

Abstract

This work presents results obtained from the production of low-cost carbons from expanded graphite (EG) and pinecone (PC) biomass, activated in potassium hydroxide (KOH) and finally carbonized in argon and hydrogen atmosphere. A specific surface area of 808 $m^2 g^{-1}$ and 457 $m^2 g^{-1}$ were measured for activated pinecone carbon (APC) and activated expanded graphite (AEG), respectively. The electrochemical characterization of the novel materials in a 2-electrode configuration as supercapacitor electrode shows a specific capacitance of 69 F g^{-1} at 0.5 A g^{-1}, high energy density of 24.6 Wh kg^{-1} at a power density of 400 W kg^{-1}. This asymmetric supercapacitor also exhibits outstanding stability after voltage holding at the maximum voltage for 110 h, suggesting that the asymmetric device based on different carbon materials has a huge capacity for a high-performance electrode in electrochemical applications.

Keywords: Pine cones; expanded graphite; Porous carbon; supercapacitor; energy storage; activated carbon

1. Introduction[1]

Electrochemical capacitors (ECs) (ultracapacitors or supercapacitors) [1] have evolved as important electrical energy storage systems for the development of wide range of electrical applications adopted in memory backup devices, hybrid electric vehicles (HEVs), digital and portable electronic devices, etc. [2–4]. Their attractiveness is attributed to their high power density, fast charging–discharging mechanism as well as long cycle life and high durability [5]. However, when compared with their battery counterparts, the energy density of ECs is still very low, hence efforts are being made to improve their energy densities to reach those of batteries or even higher.

To achieve this, porous carbon materials having high electrical conductivity, a high surface area with a good distribution of porosity are highly desirable [6,7]. Commonly used carbon materials include activated carbon [8], graphene [9–12], carbon nanotubes [13–15], carbide-derived carbons (CDC) [16,17], onions like carbon (OLC) [18,19], etc. prepared from different synthesis techniques such as chemical vapor deposition [20,21], arc discharge synthesis [22], laser ablation of graphitic targets [23], microemulsion polymerization of polymers [24,25], vaporization of graphite to nanodiamond [26] and wet chemical techniques such as the hummers method [27].

Most of the commercially available activated carbons (AC) used as electrode materials for ECs are usually prepared from coconut shells, coal, wood and peat [28–31]. More recently, attention has been shifted to the use of other sources of biomass or organic waste materials for the production of efficient, low-cost, scalable, locally available and renewable carbon materials for absorbents or energy storage application [32]. This includes materials such as

[1] The short version of the paper was presented at ICAE2016 on Oct 8-11, Beijing, China. This paper is a substantial extension of the short version of the conference paper.

waste tea-leaves [33], potato starch [34], fish scale [35], rice husk [36], waste coffee beans [37] etc. However, reports on the use of activated carbon from pine cones (PCs) for supercapacitor application are few [38,39]. PCs are in the genus Pinus family of the Pinaceae, with a major constituent of cellulose, hemicellulose, lignin, resin and tannins [40,41]. Common methods of activation of the pinecone (PC) have been extensively carried out earlier by other researchers for the production of activated carbons for absorbent applications including dye wastewaters, nitrate uptake and removal of lead (II) ions from aqueous solutions by adsorption [41–43]. There are very few reports on the use of pine cone derived carbons for energy storage applications. For example, Karthikeyan K. *et. al.* [44] reported very high surface area activated carbons synthesized from pine cone petals. Similarly, microporous carbon were derived from pinecone hull and tested as anode material for lithium batteries, which retained a discharge capacity of 357 mA h g^{-1}, and a coulombic efficiency of 98.9% at current density of 10 mA g^{-1} [44], and we recently reported a symmetric cell based on PC with energy density of 19 Wh kg^{-1} in neutral electrolyte [39]. Our choice of PC is due to the fact that they are naturally abundant in large amounts especially in Africa and many countries across the world and can be activated by a facile activation method to produce porous carbons in large quantity.

This article, demonstrate the production of high surface area porous activated carbon material by direct carbonization of chemically activated PCs and expandable graphite and further investigate its electrochemical properties as a suitable electrode for supercapacitor application. The results obtained from asymmetric supercapacitor with APC and AEG electrodes show significant improvement as a supercapacitor device.

2. Materials

Nickel foam (Alantum Innovation, Munich, Germany), Expandable graphite (grade ES 250 B5 from Qingdao Kropfmuehi Graphite), Polyvinyl alcohol (PVA) (Mw 89,000–98,000 g mol^{-1} Sigma Aldrich), Polyvinylpyrrolidone (PVP) (Mw 10,000 g mol^{-1} Sigma Aldrich), Potassium hydroxide (Sigma Aldrich), were used as received for the preparation of materials.

2.1 Material Synthesis

Activated expanded graphite (AEG) was produced according to reference [45]. Briefly, graphite sample was expanded using a microwave oven and dispersed in 100 ml of 10 wt% Polyvinylpyrrolidone (PVP) and the mixture was sonicated for 12 h. 5 g of KOH was then added to the solution, and the mixture was further stirred for 2 h at 60 ^{o}C. The solid powder obtained was dried at 70 ^{o}C for 12 h. The dried solid powder was then activated in a horizontal tube furnace ramped from room temperature to 800 ^{o}C at 5 ^{o}C/min under argon and hydrogen gas flow. This procedure transforms the EG solid precipitate into flakes of carbon material denoted as activated expanded graphite (AEG). Figure 1 presents an illustration of the procedure adopted in the production of activated pine cone carbon (APC). Briefly, The PC was crushed and then activated KOH solution with a KOH/PC mass ratio of 4:1 for 24 h and dried at 80 °C for 12 h followed by carbonization by ramping from room temperature to 800 °C at a ramp rate of 10 °C/minute, in the presence of argon and hydrogen gasses for a 2 h of carbonization. The ratio of 4:1 was chosen after a series of optimizations, and it was observed that at 800 ^{o}C the highest specific surface area with a reasonable amount of micropores needed for energy storage was attained at this ratio. Thereafter, the tube was naturally cooled down to room temperature prior to the collection

of the sample, which was washed with diluted hydrochloric acid to and deionized water before being dried.

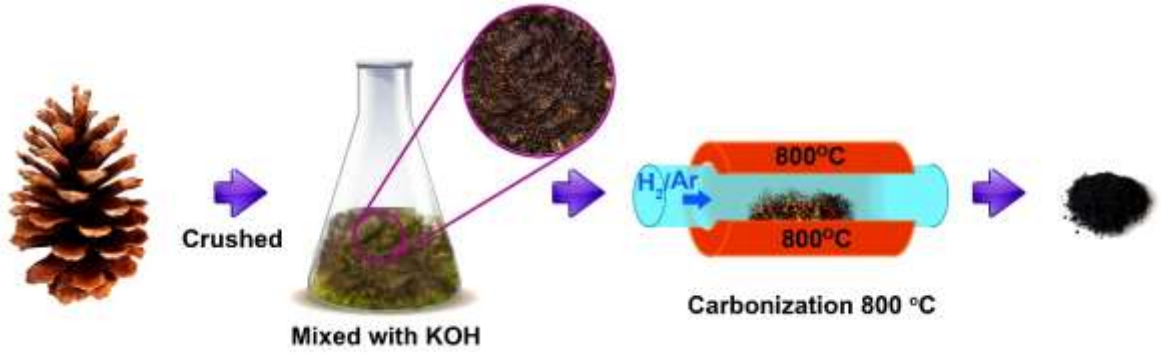

Figure 1. Schematic showing the preparation process for the synthesis of APC.

2.2. Material characterization and electrode fabrication

The scanning electron micrographs (SEM) were obtained from a Zeiss Ultra Plus 55 field emission scanning electron microscope (FE-SEM) operated at an accelerating voltage of 2.0 kV. X-ray diffraction (XRD) measurement was carried out using the XPERT-PRO diffractometer (PANalytical BV, the Netherlands) with theta/theta geometry. Qualitative phase analysis of samples was conducted using the X'pert Highscore search-match software at room temperature, while gas sorption measurement was carried out using the Micromeritics TriStar II 3020 (version 2.00) analyser, the samples were degassed at 150 °C for more than 12 h under vacuum conditions. The surface area value was obtained by the Brunauer–Emmett–Teller (BET) method. The electrodes were prepared in a similar manner to reference [37], i.e. mixing the active materials and Polytetrafluoroethylene (PTFE) as a binder with a weight ratio of 90:10, which was homogenized and dispersed in N-methyl pyrrolidone (NMP) solution. The resulting paste was then uniformly coated on a nickel foam current collector and dried at 60 °C in an oven for 8 h to ensure complete evaporation of the NMP. The electrochemical test of the symmetric cell was carried out in a two electrode cell

configuration in coin cells with a thickness of 0.2 mm and a diameter of 16 mm. A glass microfiber filter paper was used as the separator and the gel electrolyte prepared from PVA/KOH/carbon black (PKC) used as electrolyte [46] and the electrochemical measurements were carried out using a Bio-logic VMP-300 potentiostat.

3. Results and discussion

3.1 Morphology

Figure 2 (a) and (b) show the surface morphology of the pine cone before and after activation with the fibrous, cellulose like surface are observed before activation. After activation (figure 2 (b and c) low and high magnification) transforms to porous structures suitable for high-performance supercapacitors. Figure 2 (d) and (e) show the surface morphology of the expanded graphite before and after activation, showing a network of sheet-like carbon structure. The formation mechanism of porous carbons with KOH is due the carbon gasification of the sample during the activation. During the activation process, CO_2 formed from K_2CO_3 in the annealing process is released and becomes significant at high temperatures. The released CO_2 then react with hydrochar material from the pine to open up closed pores and enlarge existing micropores. On the other hand, the potassium-containing compounds, such as K_2O and K_2CO_3, can be reduced by carbon to form K metal, thus causing the carbon gasification and hence the formation of pores [47]. The activation process takes places according to the following reaction [47];

$$6KOH + C \leftrightarrow 2K + 3H_2 + 2K_2CO_3$$

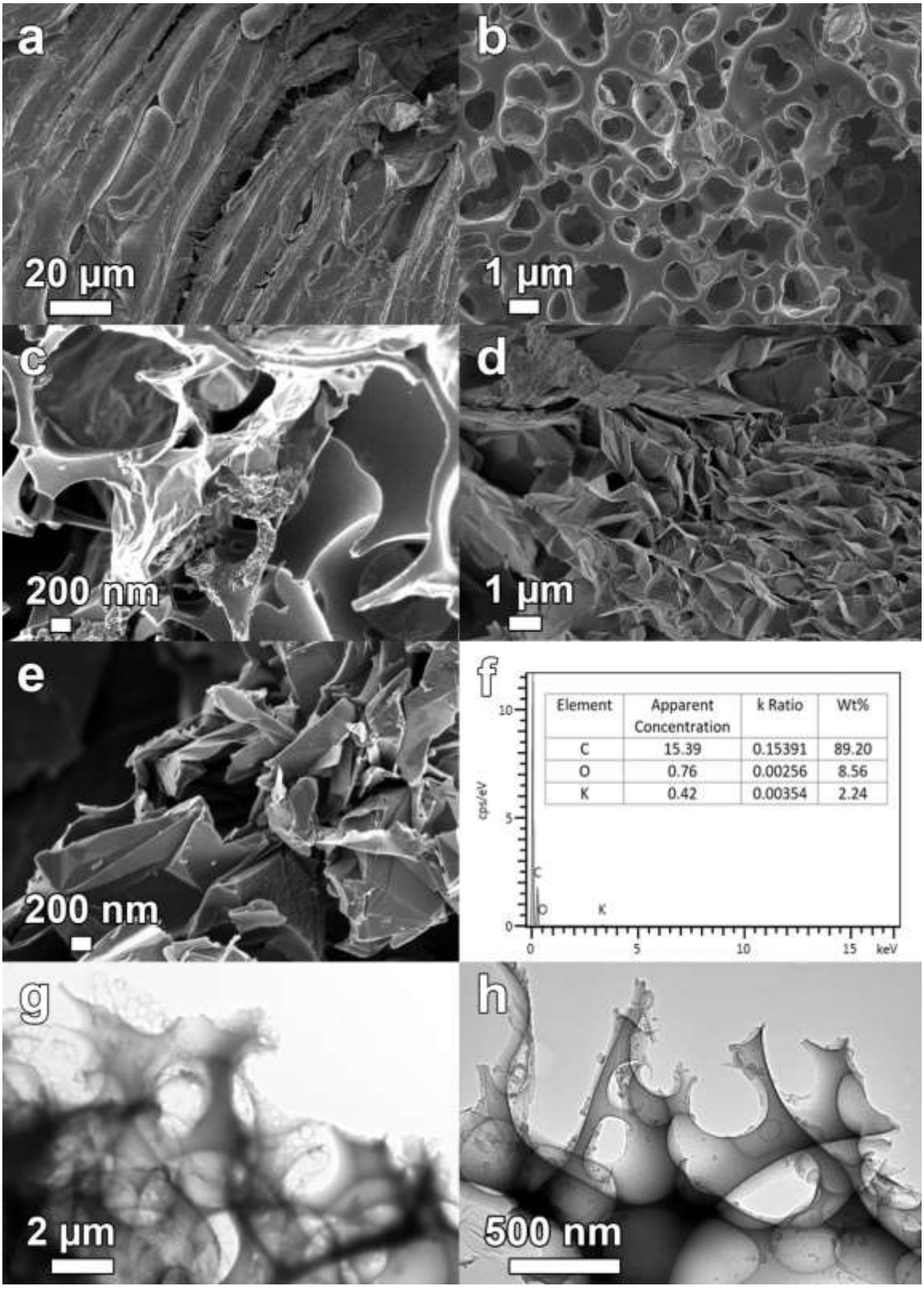

Figure 2. SEM micrographs of (a) raw pine cone, (b and c) APC (low and high magnification), (d, e) expanded graphite and AEG, (f) EDS pattern of the APC and (g and h) low and high magnification TEM of APC

Figure 2 (f) shows the EDS pattern of the APC sample predominantly showing the presence of carbon material with the highest percentage. Figure 2 (g and h) show the low and high magnification TEM consisting of highly interconnected hollow and porous spheres that overlap each other and some of the spheres are split open. The diameters of some of the spheres ranges between 100–200nm.

3.2 Structure

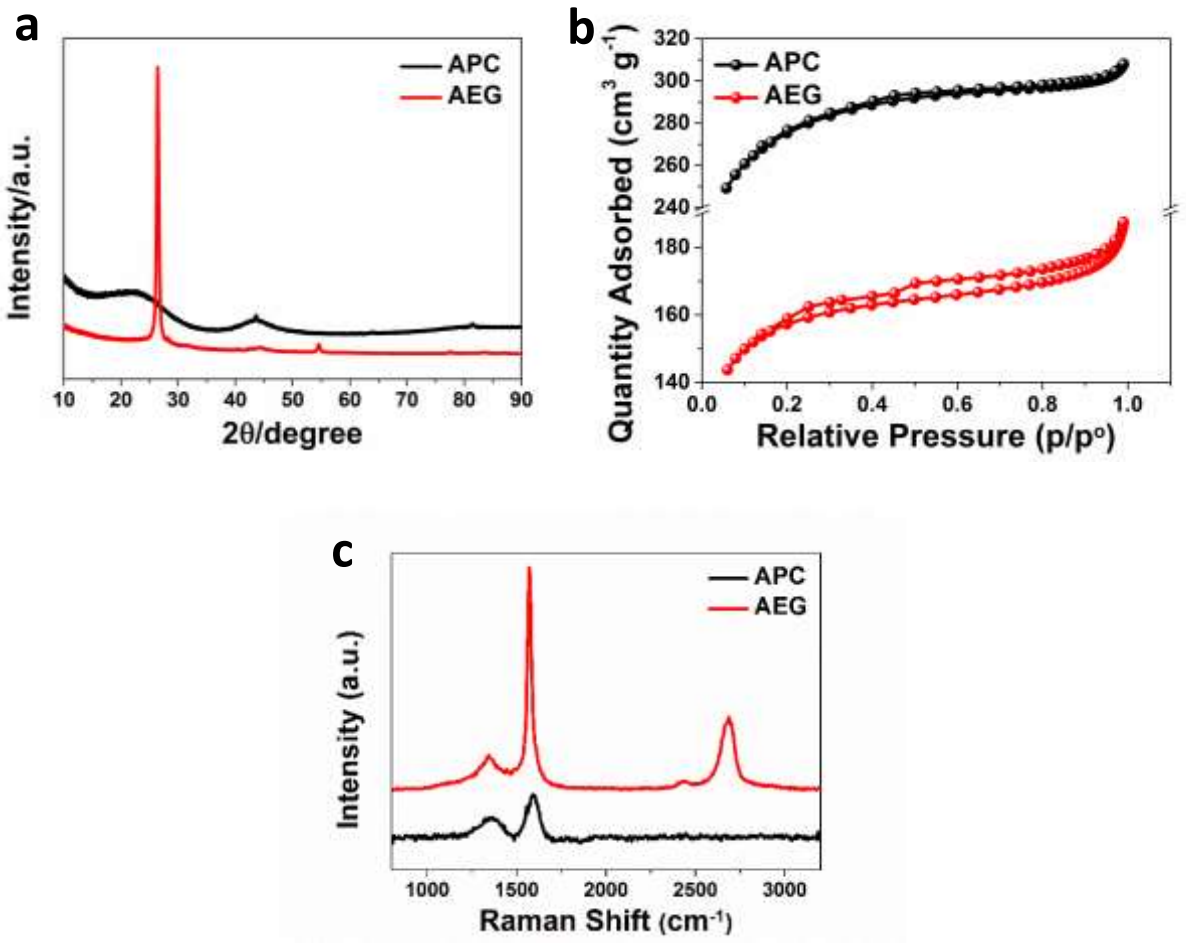

Figure 3. (a) XRD, (b) the N_2 adsorption-desorption isotherm of APC and AEG, (c) the Raman spectra of APC and AEG.

Figure 3 (a) Present the XRD results of the samples. The XRD peaks of APC (JCPDS 00-008-APC0415) are identified with graphite peaks. APC sample appears to be amorphous which is characteristic of activated carbon. In other words, a broad diffraction peak with the characteristic graphitic (carbon) peaks is recorded at a 2θ value of 26° (002). The intense graphitic peak at a 2θ value of 26° was observed in the XRD pattern of AEG sample. This suggests the high degree of crystallinity of the samples after activation [48].

The SSA of the samples was measured by the N_2 isotherms at 77 K. Figure 3 (b) shows that both samples exhibit a type II isotherm with an H4 behavior. This implies the presence of micropores and mesopores in both samples. A small hysteresis loop observed in these samples is attributed to the presence of the mesopores in the material. The BET SSA of 808 $m^2\ g^{-1}$ and 457 $m^2\ g^{-1}$ were measured for APC and AEG samples, respectively. Table 1 summarizes all the information obtained from the gas sorption analysis. From the table, the APC shows the highest micropore volume with the smallest micropore diameter. These results suggest that this material is suitable as supercapacitor electrode material. The Raman data are presented in figure 3 (c) for both carbon samples showing the presences of both the D and G peaks which are finger prints of carbon materials. The D-peak is defect induced, while the G-peak first-order Raman scattering process in carbon materials The AEG sample shows an additional peak at ~2700 cm^{-1}. This peak corresponds to the 2D overtone of the D-peak and arise due to the second-order process that involves two in-plane transverse optical mode (iTO) phonons near the K point, and the D-band from a second-order process that involves one iTO phonon and one defect [49,50]. The presence of this peak in the AEG sample shows a good degree of crystallinity when compared with APC sample.

Table 1. SSA measured parameters for the samples

Samples	Surface area (m^2/g)	micropore volume (cm^3/g)	cumulative volume (cm^3/g)	Pore diameter (nm)
APC	808	0.28	0.13	2.98
AEG	457	0.17	0.07	4.05

3.3 Electrochemical analysis

Figure 4 (a-b) show CV curves of APC and AEG electrode materials. They both reveal rectangular shapes which are a characteristic of electrical double layer capacitor (EDLC). The operating voltage for the APC electrode can withstand a potential of 1.2 V vs. Ag/AgCl in negative potential as presented in Figure 3 whereas that of AEG is 1.0 V vs. Ag/AgCl in positive potential. Figure 4 (c) shows the results of the CV plots for the APC material at 1.2 V and sweep rates from 5 to 50 m Vs^{-1}. The CV plots are characterized with no oxidation or reduction peaks corresponding to EDLC behavior. The galvanostatic charge and discharge (CD) curves are shown in Figure 4 (d), The CD lines plots are almost triangular and symmetric which indicates a fast I-V response [51]. The measured value of the specific capacitance (C_s) of the APC is 335 F g^{-1} at 0.5 A g^{-1} and decreased to 130 F g^{-1} at 10 A g^{-1} as shown in Figure 4 (e), showing a stable reduction in the capacitance of the APC electrode material with a considerable high increase in current density. Figure 4 (f) demonstrates the stability of the electrode material by subjecting it to continuous charging and discharging over several cycles. The APC shows no capacitance loss after 10000 cycles. Only a small rise in the capacitance (~2.8 %) was observed, similar to observations made in Ref. [52], which was attributed to the possible bulging of the active material due to the presence of defects, which promotes electrolyte ions intercalation into the space generated by the bulging. This

leads to an extra accessible specific surface area (SSA) and hence rise in the efficiency of the cell [52].

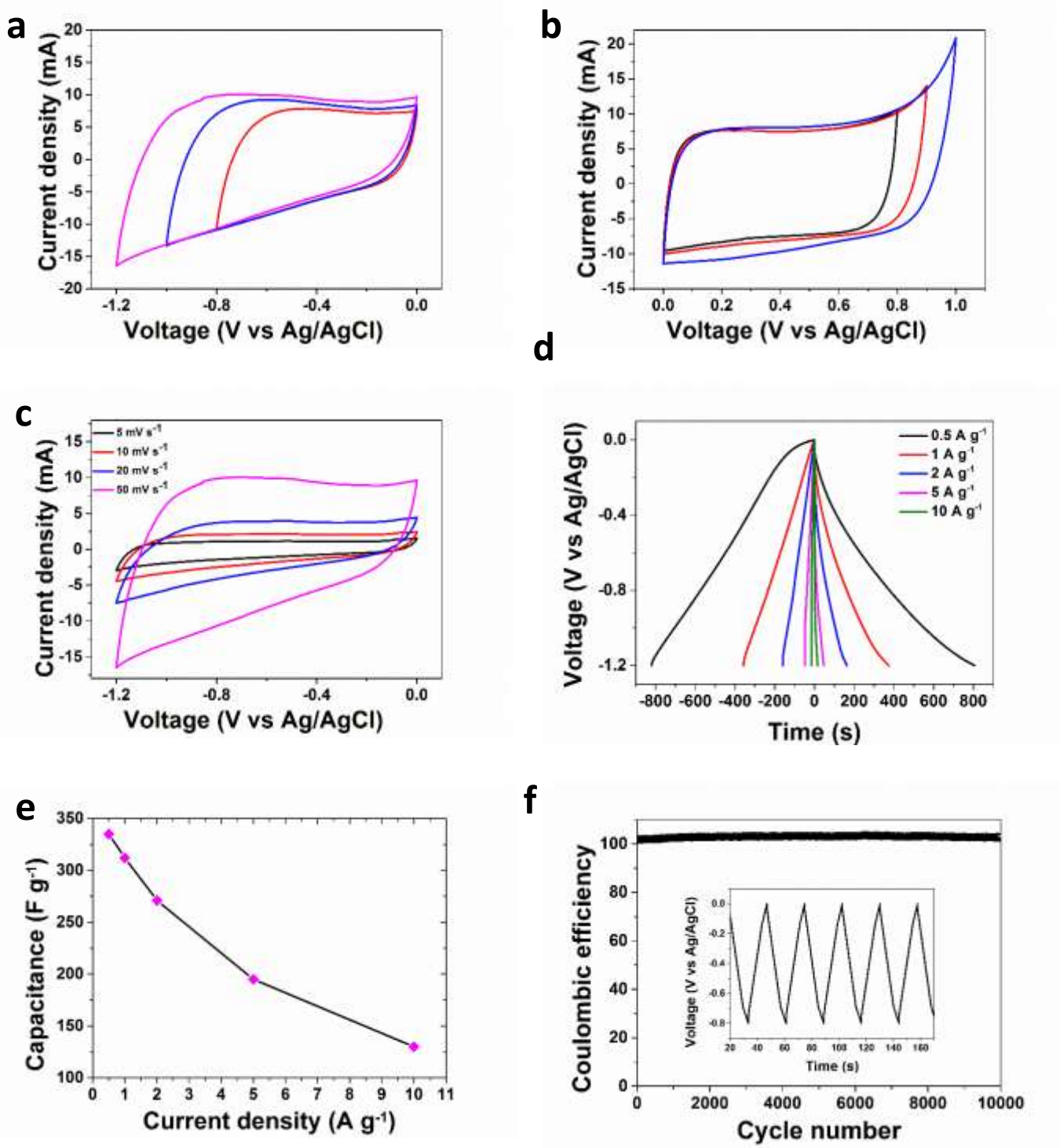

Figure 4. (a) CV of APC at different voltage windows in three electrodes in the negative potential window, (b) CV of AEG at different potential windows in the positive, (c) CV curves at different scan rates, (d) the CD curves at different current densities (e) the specific capacitance vs. current density (f) Stability at 2 A g^{-1} for APC

EIS was used to study the rate capability of the electrodes. The Nyquist plot of the electrode material is shown in Figure 5 (a). The EIS plot shows a semi-circle and a sloping line at both high and low-frequency regions respectively. The intercept on the X - axis signified by R_S represents the combined resistance of the electrolyte and all the components present in the cell such as the electrodes, separators and metallic casing. R_S value of 0.35 Ω was obtained which shows a good conductivity and high quality of the electrodes [53]. The diameter of the semi-circle (clearly shown as an inset to the figure) is the charge transfer resistance (R_{CT}) with a value of 2.1 Ω which is attributed to the double layer capacitance (C_{DL}) and the redox reaction that might occur at the surface of the electrode material. However, the resulting curve shows a deviation from the theoretical behavior (parallel line) which is due to the presence of leakage current denoted by R_L. The impedance spectrum was further analyzed with the complex nonlinear least-squares (CNLS) fitting method using the ZFIT software and the circuit as shown in the inset to Figure 5 (a) based on the equivalent RC model. The obtained plot also shows that the model used fits well with the experimental data. The capacitance vs frequency (Figure 5 (b)) was also used to check the charge propagation of the electrode material. From figure 5 (b) above, the C' of the cell is 0.15 F while C" which defines a relaxation time of ~4.3 [54].

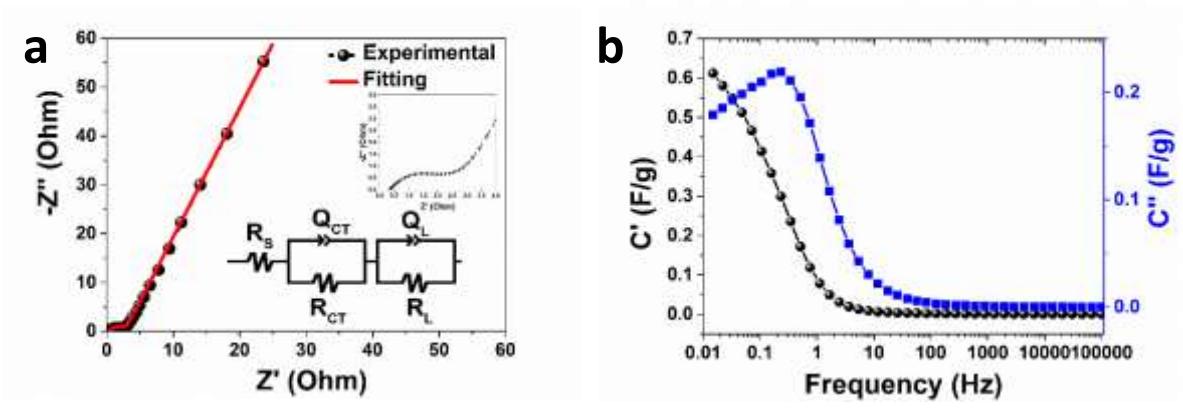

Figure 5. (a) Nyquist plot and fitting curve with the circuit and (b) the C' and C" vs. frequency of APC

Figure 6 (a) shows the two-electrode asymmetric CV consisting of APC as a negative electrode and AEG as the positive electrode. The safe potential window chosen for this cell was 1.6 V. The CV curves at this voltage preserved the rectangular shape demonstrating the capacitive behavior and high reversibility of the fabricated device. The shape of the CVs is still preserved at higher scan rates, signifying good rate capability and fast ions transportation. The charge/discharge (CD) profiles are presented in Figure 6 (b). The CD profiles show asymmetrical triangular shape, similar to the CD of symmetric supercapacitor based on AEG [45].

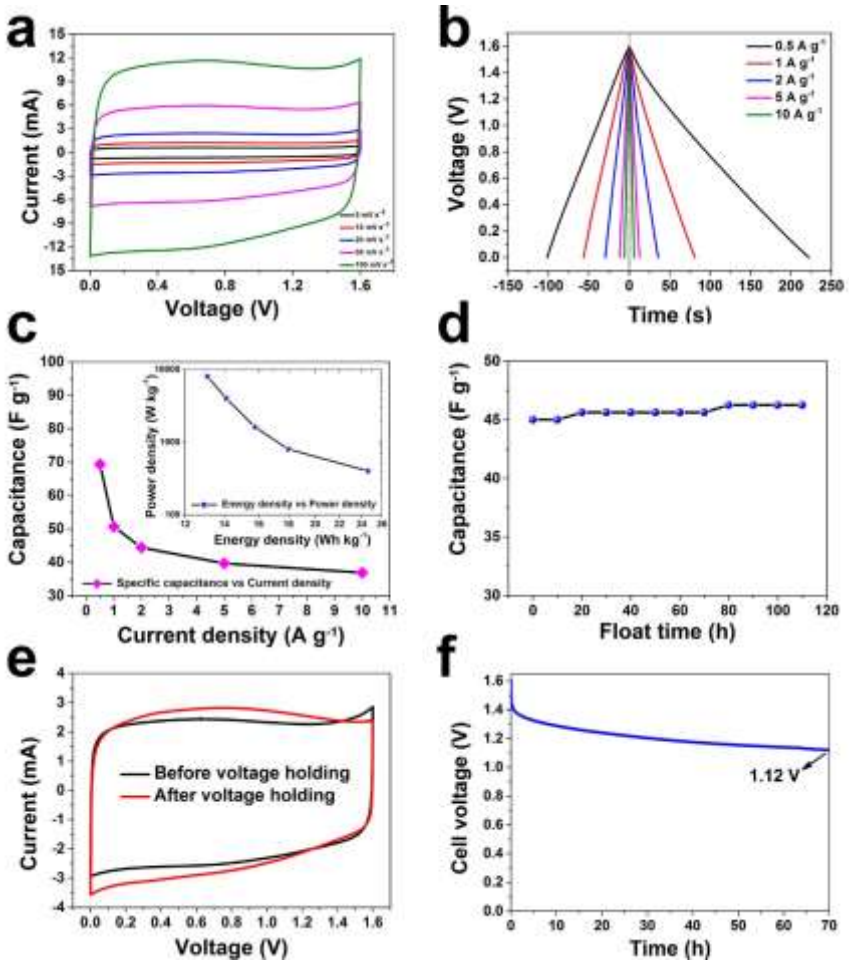

Figure 6. Electrochemical results of the fabricated device (a) CV from 5 - 100 m Vs^{-1}, (b) The CD profiles from 0.5 - 10 A g^{-1}, (c) the C_{SP} vs. the current density and Ragone plot, (d) floating time vs. C_{SP} at 2 A g^{-1}, (e) CV before and after cycling at 20 mV s^{-1} and (f) Self-discharge of the asymmetric capacitor curves after the devices were charged at 1 A g^{-1}.

The corresponding electrode C_{SP} vs. the current density and Ragone plot (Figure 6 (c)) of the device is obtained from the equations below [55–57]:

$$C_{sp} = (\mathrm{I}\,\Delta t)/M\,\Delta V \quad (1)$$

$$E_{max} = 0.5\,C(\Delta V)^2 = 1000(C_{sp} \times \Delta V^2)/(2 \times 3600) = (C_{sp} \times \Delta V^2)/7.2 \quad (2)$$

$$P_{max} = (3600 \times E_{max})/(\Delta t \times 1000) = 3.6 \times E_{max}/\Delta t \quad (3)$$

where C_{sp} is the specific capacitance, E_{max}, the energy density, P_{max}, the power density, Δt is the discharge time (s), I is the current (A), ΔV is the voltage window (V) and M is the total mass of the active material in both electrodes (g). In the design of an asymmetric cell, the voltage is dependent on the capacitance of the individual electrode materials. Thus, it imperative to take care of the charge equality: $Q_+ = Q_-$, where Q_+ and Q_- are the charges in both electrodes [58]. The loaded active mass was 2 mg for the cell. The fabricated device had a C_{SP} of 69 F g^{-1} at of 0.5 A g^{-1}, energy density of 24.6 Wh kg^{-1} at 400 W kg^{-1}. These result are superior to previous published supercapacitor results as shown in table 2 below.

Table 2. Performance comparison of this work with previous published work

Precursor	Potential (V)	Capacitance (F g^{-1})	Scan rate	Electrolyte	Energy (W h kg^{-1})	Ref.
Birnessite-type manganese oxide/AC	1.8	27.3	1 mV s^{-1}	1 M Na_2SO_4	9.4	[59]
Bamboo	3.5	146	0.2 A g^{-1}	EMIM TFSI	6.1	[60]
Poly(vinylidene chloride) (PVDC)	4	38	1 mV s^{-1}	1M $TEABF_4$ in PC	-	[61]
Polypyrrole (PPy)	2.3	290	0.1 A g^{-1}	$EMImBF_4$	-	[62]
Coal tar pitch	1	224	0.1 A g^{-1}	6M KOH	7.8	[63]
Phenol-formaldehyde resin	1.3	105	-	1M H_2SO_4	-	[64]
APC/AEG	1.6	69	0.5 A g^{-1}	Gel electrolyte	24.6	This work-

Figure 6 (d) shows the cycling test based on floating test to evaluate the stability of the device. Floating test can be described by the ageing phenomenon, i.e. a 10 h period of holding, followed by ten CD at 2 A g^{-1} and capacitance is calculated from the tenth discharge. This sequence is repeated 11 times, i.e. for a total floating time of 110 h. During floating an increase in the capacitance was observed, which is attributed to the incorporation of the ion into the matrix of the electrode at the early stage of floating and the C_{SP} remains stable after 2.7% of capacitance increase after 110 h. Figure 6 (e) present the CV curves at 20 mV s^{-1} before and after floating test with improved CV shape indicating improved rate capability with a small current rise at the negative potential ascribed to H_2 evolution.

Figure 7 (a) shows the self-discharge curve of the device recorded after it was charged to 1.6 V at 1 A g^{-1}. After 70 h, the cell still maintains a significantly high voltage value of 1.12 V. This slow self-discharge process suggests a good practical application of the supercapacitor. The quick drop of the cell voltage at the initial stage of the self-discharge is probably due to the decomposition of the solvent which is water in this case, as explained by Chen *et al.* [65]. Briefly, the solvent can be reduced on the cathode when the cell is fully charged above the thermodynamic stability potential of water (1.23 V). This reduction can go on even after current cut-off, leading to a quick decrease in the cathode potential. This procedure is influenced by the surface property of the electrode and is not diffusion controlled neither due to current leakage. Therefore, any investigation of the self-discharge mechanism will exclude this potential drop.

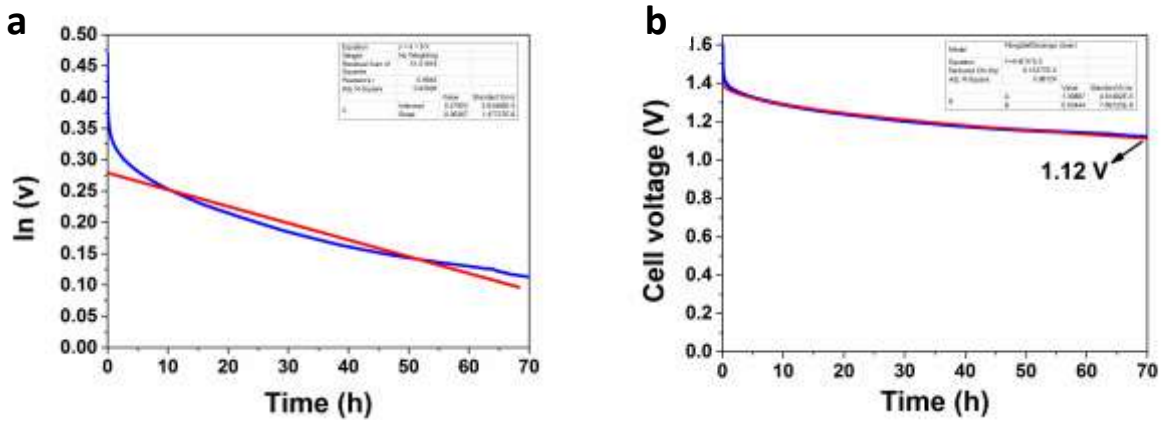

Figure 7. Fitting self-discharging with (a) current leakage over a resistance model and, (b) diffusion-control process model

To establish the major mechanism dictating the self-discharge, two well-accepted models were considered. The first model relates to the self-discharge of the supercapacitor to current leakage over a resistance R, using equation 4:

$$V = V_0 exp^{(\frac{-t}{RC})} \quad (4)$$

Where V_0 is the initial voltage of the device and C is the equivalent capacity of the supercapacitor. Thus the plot of lnV vs t should give a linear trend. However, our result deviates from this linear behavior Figure 7 (a). This implies that the self-discharge observed here is not caused by current leakage through a resistance. The second model is based on diffusion-control process. In other words, the stored charges are lost due to out-diffusion of the electrolyte ions in the electrical double layer. The voltage drop of this diffusion process is dictated by the following equation 5:

$$V = V_0 - mt^{1/2} \quad (5)$$

where m is the diffusion, which is related to the initial voltage V_0. Our data fit well this model Figure 7 (b), showing that the dominant mechanism influencing the self-discharge is diffusion control of the electrolyte ions from the electrical double layer capacitor.

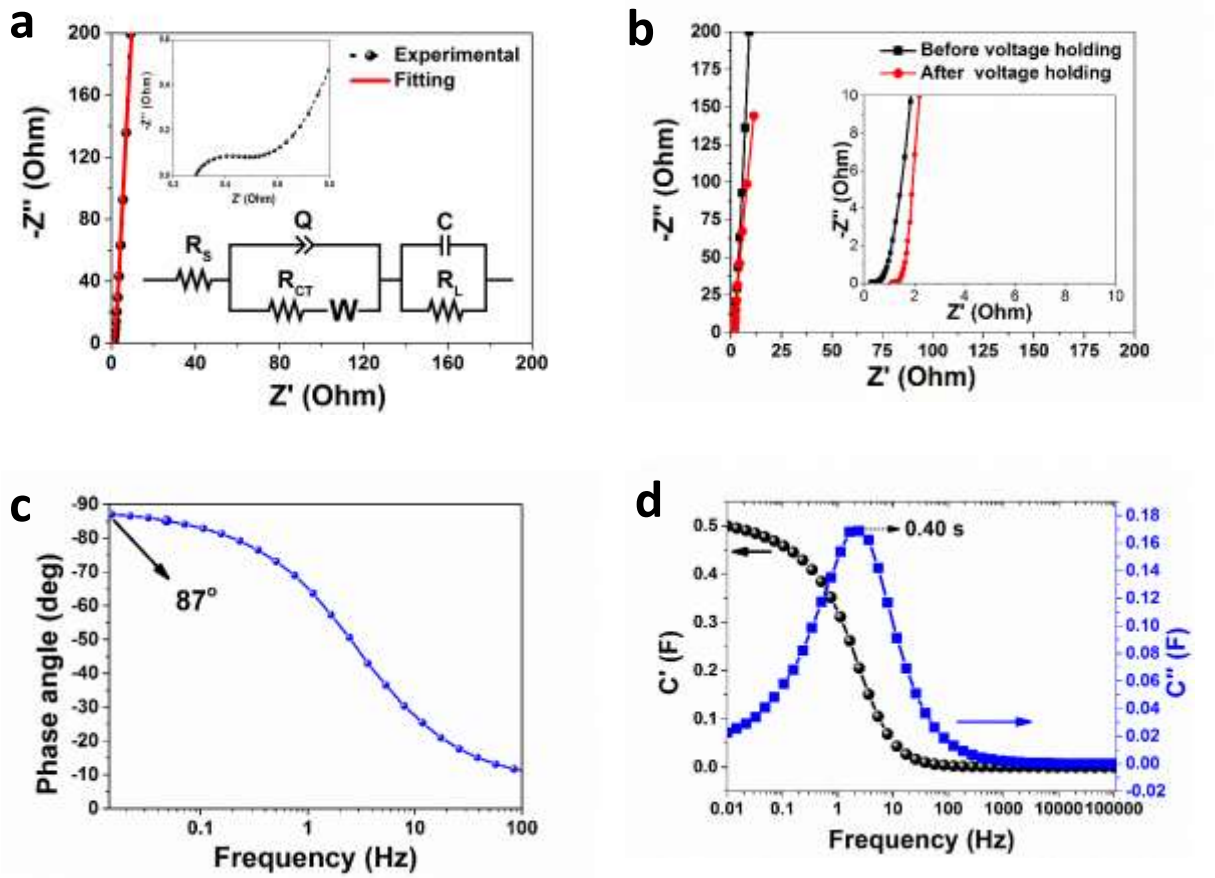

Figure 8. EIS results (a) Nyquist plot and fitting, (b) Nyquist plot prior to and after floating test, (c) the Phase angle as a function of frequency and (d) C' and C".

The device also shows markedly high electrical conductivity, suggested by the EIS results (Figure 8 (a)). Figure 8 (a) present the Nyquist plot of the device and its corresponding equivalent circuit as an inset. At the high frequency, the equivalent series resistance (ESR or R_s) is the intercept to the x-axis. The ESR includes all the resistance present in the device such as the electrolyte resistance, the resistance between the contact and the electrode materials. At the mid-frequency region, a small semicircle (inset to Figure 8 (a)) is observed owing to the charge transfer resistance and mass transport across the framework of the

porous material and is depicted by (R_{ct}). At the low-frequency region, the curve displays a line almost perpendicular to the y-axis signifying an ideal behavior of the device. However, there is a divergence from this ideal behaviour. This divergence is attributed to the existence of a resistive element associated with C. This resistance is denoted as leakage resistance R_L and is in parallel with C. The aberration from the perfect line perpendicular to the y-axis is ascribed to a diffusion process that takes place at the porous electrode-electrolyte interface and is usually characterized by the existence of a Warburg impedance element denoted by W [66]. Ideally, the phase angle of the Warburg impedance is -45°, since it represents a vector with equal real and imaginary amplitudes. In practice, a deviation from that phase angle is noticed and it has been attributed to porous nature of the electrode materials with different pore dimensions which play crucial role in the impedance analysis, for example, Song *et al.* [67], simulated the effect of pore size distribution of the EIS and it was observed that the Warburg impedance at low frequency clearly depends on the porous size distributions.

The inset to the figure presents the RC circuit. The R_s is linked in series with the capacitance, which is placed in parallel with the R_{ct}. The changeover from high to low frequency is modelled by Warburg element which is in series with R_{ct}. A perfect device in principle will give a vertical line parallel to the Y-axis at a low frequency that which is modelled by C_2 in the circuit diagram. The R_s and R_{ct} values recorded for the device are 0.28 Ω and 0.25 Ω, respectively, which are small compared with what is obtainable in the literature. However, after floating, the electrical conductivity of the cell degrades with increasing R_s and R_{ct} values to 1.1 Ω and 2.4 Ω, respectively due to the presence of hydrogen evolution. This is accompanied by the increase in the diffusion length. The resistance values obtained after

floating measurements are still significantly lower compared to a recent report based on biomass derived hierarchical carbon nanostructures with resistance value of ~4 Ω [68], suggesting the attractive electrical properties of the materials used in this cell. The phase angle as a function of the frequency presents a phase angle of -87° at low frequency (Figure 8 (c)), which is very close to phase angle of -90° for ideal capacitive behavior. Furthermore, the cell shows an appealing time constant as low as 400 ms which corresponds to the characteristic frequency at -45°. This value is much lower than value reported by Zhu *et al.* [68] who found a time constant value of 900 ms for biomass-derived hierarchical carbon nanostructures and even significantly lower than that of activated carbon (10 s) [69,70]

5. Conclusion

Low-cost porous carbon prepared from expanded graphite and pinecone with SSA of 457 m^2 g^{-1} and 808 m^2 g^{-1}, respectively were tested as active electrode materials for supercapacitor. An asymmetric device fabricated shows a C_{SP} of 69 F g^{-1} at 0.5 A g^{-1} with an energy density of 24.6 Wh kg^{-1} at a power density of 400 W kg^{-1}. This asymmetric device also displays excellent stability after 110 h of voltage holding in gel electrolyte, demonstrating that asymmetric configurations based on different carbon material hold a great potential for improved electrochemical performance in electrochemical energy storage. This work demonstrated the use of abundant biomass as raw material for the synthesis of AC with good electrochemical properties. The long self-discharge time is very interesting for this material; however, the specific capacitance will need to be improved by functionalizing the material. Supercapacitor based on renewable pinecone can be used for energy saving and reduction of power peak demand in electronic device [71] and also can be used in battery/supercapacitor hybrid energy storage system for electric vehicles [72,73]. In the

future, this cell could also be tested in an Ionic liquid or organic electrolyte with wider working potential in order to further enhance the energy density of the cell.

ACKNOWLEDGEMENT

This research is supported by the National Research Foundation of South Africa (Grant Numbers: 61056). The finding and conclusion or recommendation expressed in this work is that of the author(s) and the NRF does not accept any liability in this regard.

REFERENCES

[1] Burke A. Ultracapacitors: Why, how, and where is the technology. J Power Sources 2000;91:37–50.

[2] Miller JR, Simon P. Materials science. Electrochemical capacitors for energy management. Science 2008;321:651–2.

[3] Kötz R, Kötz R, Carlen M, Carlen M. Principles and applications of electrochemical capacitors. Electrochim Acta 2000;45:2483–98.

[4] Gromadskyi DG, Chae JH, Norman SA, Chen GZ. Correlation of energy storage performance of supercapacitor with iso-propanol improved wettability of aqueous electrolyte on activated carbon electrodes of various apparent densities. Appl Energy 2015;159:39–50.

[5] Bose S, Kuila T, Mishra AK, Rajasekar R, Kim NH, Lee JH. Carbon-based nanostructured materials and their composites as supercapacitor electrodes. J Mater Chem 2012;22:767–84.

[6] Zhang C, Hatzell KB, Boota M, Dyatkin B, Beidaghi M, Long D, et al. Highly porous carbon spheres for electrochemical capacitors and capacitive flowable suspension electrodes. Carbon 2014;77:155–64.

[7] Simon P, Gogotsi Y. Materials for electrochemical capacitors. Nat Mater 2008;7:845–54.

[8] Pandolfo AG, Hollenkamp AF. Carbon properties and their role in supercapacitors. J Power Sources 2006;157:11–27.

[9] Zhang LL, Zhou R, Zhao XS. Graphene-based materials as supercapacitor electrodes. J Mater Chem 2010;20:5983–92.

[10] Stoller M, Park S, Zhu Y, An J, Ruoff R. Graphene-based ultracapacitors. Nano Lett 2008;8:3498–502.

[11] Lee YR, Kim SC, Lee H, Jeong HM, Raghu A V., Reddy KR, et al. Graphite oxides as effective fire retardants of epoxy resin. Macromol Res 2011;19:66–71.

[12] Lee MS, Choi H-J, Baek J-B, Chang DW. Simple solution-based synthesis of pyridinic-rich nitrogen-doped graphene nanoplatelets for supercapacitors. Appl Energy 2017;195:1071–8.

[13] Henrik Staaf, Amin M Saleem, Gert Göransson, Per Lundgren PE. Carbon nanotubes as electrode for supercapacitors. 2nd Int. Conf. Mater. Energy, May 12-16, 2013 Karlsruhe, Ger., 2013.

[14] Frackowiak E, Metenier K, Bertagna V, Beguin F. Supercapacitor electrodes from multiwalled carbon nanotubes. Appl Phys Lett 2000;77:2421.

[15] Li Y-H, Li Q-Y, Wang H-Q, Huang Y-G, Zhang X-H, Wu Q, et al. Synthesis and electrochemical properties of nickel–manganese oxide on MWCNTs/CFP substrate as a supercapacitor electrode. Appl Energy 2015;153:78–86.

[16] Chmiola J, Largeot C, Taberna P-L, Simon P, Gogotsi Y. Monolithic carbide-derived carbon films for micro-supercapacitors. Science 2010;328:480–3.

[17] Arulepp M, Leis J, Lätt M, Miller F, Rumma K, Lust E, et al. The advanced carbide-derived carbon based supercapacitor. J Power Sources 2006;162:1460–6.

[18] Pech D, Brunet M, Durou H, Huang P, Mochalin V, Gogotsi Y, et al. Ultrahigh-power micrometre-sized supercapacitors based on onion-like carbon. Nat Nanotechnol 2010;5:651–4.

[19] Bushueva EG, Galkin PS, Okotrub A V., Bulusheva LG, Gavrilov NN, Kuznetsov VL, et al. Double layer supercapacitor properties of onion-like carbon materials. Phys Status Solidi 2008;245:2296–9.

[20] Wei D, Liu Y, Wang Y, Zhang H, Huang L, Yu G. Synthesis of N-doped graphene by chemical vapor

deposition and its electrical properties. Nano Lett 2009;9:1752–8.

[21] Li X, Cai W, An J, Kim S, Nah J, Yang D, et al. Large-area synthesis of high-quality and uniform graphene films on copper foils. Science 2009;324:1312–4.

[22] Qin Z, Li ZJ, Yang BC. Synthesis of carbon nanowires as electrochemical electrode materials. Mater Lett 2012;69:55–8.

[23] Kong X, Huang Y, Chen Y. Difference in formation of carbon cluster cations by laser ablation of graphene and graphene oxide. J Mass Spectrom 2012;47:523–8.

[24] Hassan M, Reddy KR, Haque E, Faisal SN, Ghasemi S, I. Minett A, et al. Hierarchical assembly of graphene/polyaniline nanostructures to synthesize free-standing supercapacitor electrode. Compos Sci Technol 2014;98:1–8.

[25] Reddy KR, Sin BC, Ryu KS, Noh J, Lee Y. In situ self-organization of carbon black–polyaniline composites from nanospheres to nanorods: Synthesis, morphology, structure and electrical conductivity. Synth Met 2009;159:1934–9.

[26] Tian F, Yang H, Zhao YG, Cao HM. Size Effect on the Transformation from Graphite to Nanodiamonds. Mater. Sci. Forum, vol. 787, 2014, p. 412–8.

[27] Jr WH, Offeman R. Preparation of graphitic oxide. J Am Chem Soc 1958;80:1339–1339.

[28] Yang K, Peng J, Srinivasakannan C, Zhang L, Xia H, Duan X. Preparation of high surface area activated carbon from coconut shells using microwave heating. Bioresour Technol 2010;101:6163–9.

[29] Ge X, Tian F, Wu Z, Yan Y, Cravotto G, Wu Z. Adsorption of naphthalene from aqueous solution on coal-based activated carbon modified by microwave induction: Microwave power effects. Chem Eng Process Process Intensif 2015;91:67–77.

[30] Acevedo B, Barriocanal C, Lupul I, Gryglewicz G. Properties and performance of mesoporous activated carbons from scrap tyres, bituminous wastes and coal. Fuel 2015;151:83–90.

[31] Salame II, Bandosz TJ. Surface Chemistry of Activated Carbons: Combining the Results of Temperature-Programmed Desorption, Boehm, and Potentiometric Titrations. J Colloid Interface Sci 2001;240:252–

8.

[32] Park S, Liang C, Sheng D, Dudney N, DePaoli D. Mesoporous Carbon Materials as Electrodes for Electrochemical Double-Layer Capacitor. MRS Proc 2006;973:903–16.

[33] Peng C, Yan X, Wang R, Lang J, Ou Y, Xue Q. Promising activated carbons derived from waste tea-leaves and their application in high performance supercapacitors electrodes. Electrochim Acta 2013;87:401–8.

[34] Zhao S, Wang C-Y, Chen M-M, Wang J, Shi Z-Q. Potato starch-based activated carbon spheres as electrode material for electrochemical capacitor. J Phys Chem Solids 2009;70:1256–60.

[35] Chen W, Zhang H, Huang Y, Wang W. A fish scale based hierarchical lamellar porous carbon material obtained using a natural template for high performance electrochemical capacitors. J Mater Chem 2010;20:4773–5.

[36] Yuan C, Lin H, Lu H, Xing E, Zhang Y, Xie B. Synthesis of hierarchically porous MnO2/rice husks derived carbon composite as high-performance electrode material for supercapacitors. Appl Energy 2016;178:260–8.

[37] Rufford TE, Hulicova-Jurcakova D, Zhu Z, Lu GQ. Nanoporous carbon electrode from waste coffee beans for high performance supercapacitors. Electrochem Commun 2008;10:1594–7.

[38] Manyala N, Bello A, Barzegar F, Khaleed AA, Momodu DY, Dangbegnon JK. Coniferous pine biomass: A novel insight into sustainable carbon materials for supercapacitors electrode. Mater Chem Phys 2016;182:139–47.

[39] Bello A, Manyala N, Barzegar F, Khaleed AA, Momodu DY, Dangbegnon JK, et al. Renewable pine cone biomass derived carbon materials for supercapacitor application. RSC Adv 2016;6:1800–9.

[40] ROBBINS WW, WEIER TE, STOCKING CR. Botany:An Introduction to Plant Science. Soil Sci 1957;84:180.

[41] Ofomaja AE, Naidoo EB. Biosorption of copper from aqueous solution by chemically activated pine cone: A kinetic study. Chem Eng J 2011;175:260–70.

[42] Nunell G V, Fernandez ME, Bonelli PR, Cukierman AL. Nitrate uptake improvement by modified

activated carbons developed from two species of pine cones. J Colloid Interface Sci 2015;440:102–8.

[43] Momčilović M, Purenović M, Bojić A, Zarubica A, Ranđelović M. Removal of lead(II) ions from aqueous solutions by adsorption onto pine cone activated carbon. Desalination 2011;276:53–9.

[44] Karthikeyan K, Amaresh S, Lee SN, Sun X, Aravindan V, Lee Y-G, et al. Construction of High-Energy-Density Supercapacitors from Pine-Cone-Derived High-Surface-Area Carbons. ChemSusChem 2014;7:1435–42.

[45] Barzegar F, Bello A, Momodu D, Madito MJ, Dangbegnon J, Manyala N. Preparation and characterization of porous carbon from expanded graphite for high energy density supercapacitor in aqueous electrolyte. J Power Sources 2016;309:245–53.

[46] Barzegar F, Dangbegnon JK, Bello A, Momodu DY, Johnson ATC, Manyala N. Effect of conductive additives to gel electrolytes on activated carbon-based supercapacitors. AIP Adv 2015;5:97171.

[47] Wang J, Kaskel S. KOH activation of carbon-based materials for energy storage. J Mater Chem 2012;22:23710–25.

[48] Gao W, Alemany LB, Ci L, Ajayan PM. New insights into the structure and reduction of graphite oxide. Nat Chem 2009;1:403–8.

[49] Wang Y, Alsmeyer DC, McCreery RL. Raman spectroscopy of carbon materials: Structural basis of observed spectra. Chem Mater 1990;2:557–63.

[50] Cuesta A, Dhamelincourt P, Laureyns J, Martínez-Alonso A, Tascón JMD. Raman microprobe studies on carbon materials. Carbon 1994;32:1523–32.

[51] Zhang W, Ma C, Fang J, Cheng J, Zhang X, Dong S, et al. Asymmetric electrochemical capacitors with high energy and power density based on graphene/CoAl-LDH and activated carbon electrodes. RSC Adv 2013;3:2483–90.

[52] Ren G, Pan X, Bayne S, Fan Z. Kilohertz ultrafast electrochemical supercapacitors based on perpendicularly-oriented graphene grown inside of nickel foam. Carbon 2014;71:94–101.

[53] Zhi M, Yang F, Meng F, Li M, Manivannan A, Wu N. Effects of Pore Structure on Performance of An

Activated-Carbon Supercapacitor Electrode Recycled from Scrap Waste Tires. ACS Sustain Chem Eng 2014;2:1592–8.

[54] Taberna PL, Simon P, Fauvarque J-FF. Electrochemical Characteristics and Impedance Spectroscopy Studies of Carbon-Carbon Supercapacitors. J Electrochem Soc 2003;150:A292-300.

[55] Stoller MD, Ruoff RS. Best practice methods for determining an electrode material's performance for ultracapacitors. Energy Environ Sci 2010;3:1294–301.

[56] Gogotsi Y, Simon P. True performance metrics in electrochemical energy storage. Science 2011;334:917–8.

[57] Demarconnay L, Raymundo-Piñero E, Béguin F. Adjustment of electrodes potential window in an asymmetric carbon/MnO2 supercapacitor. J Power Sources 2011;196:580–6.

[58] Barzegar F, Bello A, Momodu DY, Dangbegnon JK, Taghizadeh F, Madito MJ, et al. Asymmetric supercapacitor based on an α-MoO 3 cathode and porous activated carbon anode materials. RSC Adv 2015;5:37462–8.

[59] Liu H, Zhao K. Asymmetric flow electrochemical capacitor with high energy densities based on birnessite-type manganese oxide nanosheets and activated carbon slurries. J Mater Sci 2016;51:9306–13.

[60] Tian W, Gao Q, Tan Y, Yang K, Zhu L, Yang C, et al. Bio-inspired beehive-like hierarchical nanoporous carbon derived from bamboo-based industrial by-product as a high performance supercapacitor electrode material. J Mater Chem A 2015;3:5656–64.

[61] Kim Y., Horie Y, Ozaki S, Matsuzawa Y, Suezaki H, Kim C, et al. Correlation between the pore and solvated ion size on capacitance uptake of PVDC-based carbons. Carbon 2004;42:1491–500.

[62] Wei L, Sevilla M, Fuertes AB, Mokaya R, Yushin G. Polypyrrole-Derived Activated Carbons for High-Performance Electrical Double-Layer Capacitors with Ionic Liquid Electrolyte. Adv Funct Mater 2012;22:827–34.

[63] He X, Li R, Qiu J, Xie K, Ling P, Yu M, et al. Synthesis of mesoporous carbons for supercapacitors from coal tar pitch by coupling microwave-assisted KOH activation with a MgO template. Carbon

2012;50:4911–21.

[64] Teng H, Chang Y-J, Hsieh C-T. Performance of electric double-layer capacitors using carbons prepared from phenol–formaldehyde resins by KOH etching. Carbon 2001;39:1981–7.

[65] Chen L, Bai H, Huang Z, Li L. Mechanism investigation and suppression of self-discharge in active electrolyte enhanced supercapacitors. Energy Environ Sci 2014;7:1750–9.

[66] Li H, Wang J, Chu Q, Wang Z, Zhang F, Wang S. Theoretical and experimental specific capacitance of polyaniline in sulfuric acid. J Power Sources 2009;190:578–86.

[67] Song H-K, Jung Y-H, Lee K-H, Dao LH. Electrochemical impedance spectroscopy of porous electrodes: the effect of pore size distribution. Electrochim Acta 1999;44:3513–9.

[68] Zhu Z, Jiang H, Guo S, Cheng Q, Hu Y, Li C. Dual Tuning of Biomass-Derived Hierarchical Carbon Nanostructures for Supercapacitors: the Role of Balanced Meso/Microporosity and Graphene. Sci Rep 2015;5:15936.

[69] El-Kady MF, Strong V, Dubin S, Kaner RB. Laser scribing of high-performance and flexible graphene-based electrochemical capacitors. Science 2012;335:1326–30.

[70] El-Kady MF, Kaner RB. Scalable fabrication of high-power graphene micro-supercapacitors for flexible and on-chip energy storage. Nat Commun 2013;4:1475.

[71] Ciccarelli F, Iannuzzi D, Tricoli P. Control of metro-trains equipped with onboard supercapacitors for energy saving and reduction of power peak demand. Transp Res Part C Emerg Technol 2012;24:36–49.

[72] Jian Cao, Emadi A. A New Battery/UltraCapacitor Hybrid Energy Storage System for Electric, Hybrid, and Plug-In Hybrid Electric Vehicles. IEEE Trans Power Electron 2012;27:122–32.

[73] Khosrozadeh A, Xing M, Wang Q. A high-capacitance solid-state supercapacitor based on free-standing film of polyaniline and carbon particles. Appl Energy 2015;153:87–93.